ROYAL SOCIETY
OF CHEMISTRY

PAPER

Glucose-assisted synthesis of the hierarchical TiO₂ nanowire@MoS₂ nanosheet nanocomposite and its synergistic lithium storage performance†

Xiaodan Li,‡[ab] Wei Li,‡[b] Meicheng Li,*[ac] Peng Cui,[a] Dehong Chen,[d] Thomas Gengenbach,[b] Lihua Chu,[a] Huiyuan Liu[e] and Guangsheng Song[b]

A hierarchical nanocomposite of TiO₂ nanowires decorated with molybdenum disulfide nanosheets (TiO₂@MoS₂) was synthesized by a facile and low-cost glucose-assisted hydrothermal approach. In this hierarchical nanocomposite, TiO₂ nanowires served as an effective backbone for the nucleation and growth of few layered MoS₂ nanosheets. Both glucose and the roughness of anatase-TiO₂ (B) nanowires played important roles in the formation of the uniform TiO₂ nanowire@MoS₂ nanosheet (≤6 layers) nanocomposite. A synergistic effect was demonstrated on the nanocomposite of the TiO₂ nanowire@MoS₂ nanosheet. The one-dimensional robust TiO₂ nanowire backbone provided a shortened and efficient pathway for electron and lithium ion transport and minimized the strain of the volume changes, while ultrathin MoS₂ nanosheets offered high electrode/electrolyte interfacial contact areas, promoted rapid charge transfer and contributed to a high specific capacity. The favourable synergistic effect led to enhanced specific capacity, good cycling stability and superior rate capability of the nanocomposite, compared with either individual component. Such a TiO₂ nanowire@MoS₂ nanosheet nanocomposite is a promising anode material for high performance lithium ion batteries.

Introduction

Lithium ion batteries (LIBs) have attracted worldwide attention and increasing research interest over the past decade since they exhibit high energy density and they are considered as one of the most promising energy-storage devices for electric vehicles and renewable energy.[1–4] Typically, LIBs with a graphite anode have been commercially used. However, the low theoretical capacity (372 mA h g⁻¹) of the graphite anode cannot meet the ever-growing market demand for high energy density and high power density batteries.[3,4] Over the past decades, intensive worldwide efforts have been devoted to developing novel high performance electrode materials for LIBs.[5–10] Transition metal sulphides, such as WS₂,[11] FeS[12] and MoS₂ (ref. 13 and 14) have been studied as alternative anode materials for lithium storage due to their relatively high energy density and structural advantages in reversible Li⁺ storage processes. In particular, MoS₂ has been found to be a promising anode material for LIBs due to its layered structure and the capability to allow easy lithium ion insertion/extraction, enabling its assembly with diverse substrates and delivering a high theoretical specific capacity of 670 mA h g⁻¹.[14] Various MoS₂ nanostructures such as nanoplates,[15] nanotubes[16] and nanoflowers[17] have been reported for lithium storage as LIB anodes which showed high capacities. However, large volume changes normally occur in the MoS₂-based anodes during repeated discharge and charge, which causes severe pulverization, particle aggregation and unstable solid electrolyte interphase, hence resulting in rapid capacity fading upon cycling and low Coulombic efficiencies.[15–17] These seriously impede the practical application of MoS₂ as an anode material for LIBs.

To overcome these obstacles, a promising strategy is to immobilize MoS₂ nanostructures into/onto substrate matrices to construct nanocomposites. Most of the previous studies focused on MoS₂–carbon nanocomposites, using various carbonaceous matrices including carbon nanotubes,[18,19] carbon nanofibers,[20–22] graphene[23–25] and organic conducting polymers.[26] In these nanocomposites, the synergy between MoS₂

[a]State Key Laboratory of Alternate Electrical Power System with Renewable Energy Sources, School of Renewable Energy, North China Electric Power University, Beijing 102206, China. E-mail: mcli@ncepu.edu.cn; Fax: +86 10 6177 2951; Tel: +86 10 6177 2951

[b]Commonwealth Scientific and Industrial Research Organization (CSIRO), Manufacturing Flagship, Clayton South, Victoria 3169, Australia

[c]Suzhou Institute, North China Electric Power University, Suzhou 215123, China

[d]PFPC, School of Chemistry, The University of Melbourne, Melbourne, Victoria 3010, Australia

[e]Department of Materials Engineering, Monash University, Clayton, Victoria 3800, Australia

and matrices can be demonstrated. However, the excessive interface between porous carbonaceous matrices and electrolytes gives rise to considerable side reactions, forming a thick solid electrolyte interface (SEI) on the carbon and leading to a low initial Coulombic efficiency of <70%.[18–25] Therefore, it is highly desirable to improve the performance of MoS_2 by rational design of MoS_2 based nanocomposite architectures using alternative backbone materials.

Recently, titanium dioxide (TiO_2) has been widely used as a backbone material for hybrid systems. Despite its relatively low specific capacity, TiO_2 anode materials usually display remarkable cycling stability owing to the low volume change (<4%).[27] Furthermore, TiO_2 is also abundant, low cost and non-toxic, and it is a safer material compared to graphite because of its higher operation voltage (1.7 V $vs.$ Li^+/Li).[27–31] Previous studies have shown that the one-dimensional (1D) nanostructure TiO_2 could provide relatively short path lengths for both electronic and Li ionic transport and alleviate the strain of the volume variation.[32–37] Some hybrid systems based on 1D TiO_2 nanostructures, such as $TiO_2@SnO_2$,[32] $TiO_2@Fe_2O_3$ (ref. 33 and 34) and $TiO_2@Co_3O_4$,[35] have been developed to exhibit improved electrochemical performance as an anode material for LIBs, proving the feasibility of the nanocomposite strategy. Given the complementary features of the TiO_2 and MoS_2 components, a synergistic effect may be expected on their combination.

The $TiO_2@MoS_2$ hybrid nanostructures were reported very recently.[36,37] However, the TiO_2 skeleton was synthesized by a complicated template method or an extra hydrothermal oxidation procedure with sulphuric acid treatment, which required tedious procedures and was time-consuming. Furthermore, it is not clarified that what factors determine the successful fabrication of uniform $TiO_2@MoS_2$ hybrid nanostructures.

Herein, we reported the synthesis of a hierarchical nanocomposite, in which TiO_2 nanowires were decorated with ultrathin molybdenum disulfide nanosheets ($TiO_2@MoS_2$), by a simple, scalable and economical glucose-assisted hydrothermal approach. Both glucose and the roughness of anatase-TiO_2 (B) nanowires played critical roles in the formation of the uniform TiO_2 nanowire@MoS_2 nanosheet (≤6 layers) nanocomposite. The robust TiO_2 nanowires doped with carbon acted as a backbone to provide an efficient pathway for the fast lithiation/delithiation of MoS_2 and accommodate the volume changes. Meanwhile, ultrathin MoS_2 nanosheets offered high electrode/electrolyte interfacial contact areas, promoted rapid charge transfer and contributed high specific capacities. The combination of the two components in $TiO_2@MoS_2$ integrated the robustness of TiO_2 and the high lithium storage performance of MoS_2 to demonstrate a favourable synergistic effect, resulting in a higher capacity and better cycling stability than that of either single component. The $TiO_2@MoS_2$ nanocomposite showed a high initial discharge capacity of 862 mA h g^{-1} and a high initial Coulombic efficiency of 84% at 100 mA g^{-1}. Even after 100 cycles, the discharge capacity remained at 544 mA h g^{-1} with the Coulombic efficiency of over 99%. The $TiO_2@MoS_2$ nanocomposite also displayed an excellent rate capability with a specific capacity of 414 mA h g^{-1} at 1000 mA g^{-1}.

Experimental section

Material synthesis

Chemicals. Titanium dioxide (P25), sodium hydroxide (NaOH), glucose, hydrochloric acid (HCl), sodium molybdite ($Na_2MoO_4 \cdot 2H_2O$) and thiourea (CH_4N_2S) were purchased from Sigma-Aldrich. All chemicals were used as received without further purification.

Preparation of TiO_2 nanowires. In a typical synthesis, 2 g of TiO_2 powder (P25) was mixed with 200 mL of 10 mol L^{-1} NaOH aqueous solution. The mixture solution was stirred and then transferred into a Teflon-lined stainless steel autoclave and heated at 180 °C for 24 h, followed by natural cooling to room temperature. The obtained $Na_2Ti_3O_7$ powders were washed thoroughly with deionized water followed by a filtration process and dried at 70 °C. The obtained powders were immersed in 0.1 mol L^{-1} HCl aqueous solution for 24 h. Finally, the product was separated from the solution by centrifugation, washed with deionized water to neutral pH, and dried at 70 °C for 10 h. TiO_2 nanowires (TiO_2-500C) with a rough surface were obtained by calcination of the as-prepared powders at 500 °C in air for 2 h. For comparison, smooth TiO_2 nanowires (TiO_2-800C) were also further obtained by calcination of the as-prepared powders at 800 °C for 2 h.

Preparation of the TiO_2 nanowire@MoS_2 nanosheet ($TiO_2@MoS_2$) nanocomposite. 100 mg of as-obtained porous TiO_2 nanowires (TiO_2-500C) were dispersed into the glucose solution (60 mL, 0.05 M) by ultrasonication for 5 minutes. Then, 0.6 g of sodium molybdate ($Na_2MoO_4 \cdot 2H_2O$) and 1.2 g of thiourea were added. After stirring for 5 minutes, the reaction solution was transferred into a 100 mL Teflon-lined stainless steel autoclave and kept in an electric oven at 200 °C for 24 h. The autoclave was then left to cool down to room temperature naturally. The black precipitate was collected by centrifugation, washed thoroughly with ethanol, and dried at 70 °C for 12 h. Then the resulting $TiO_2@MoS_2$ hydrothermal product was further treated at 800 °C in an atmosphere of 2% of H_2 balanced by Ar for 2 h with a heating rate of 5 °C min^{-1} to obtain the annealed $TiO_2@MoS_2$ nanocomposite.

For comparison, one control sample was synthesized by employing TiO_2-500C without the addition of glucose. The other control sample was prepared by using TiO_2-800C with the addition of glucose. Other synthesis conditions remained identical.

Preparation of MoS_2 nanosheets. Bare MoS_2 nanosheets were prepared according to the same method as mentioned above, except for the addition of TiO_2 nanowires.

Characterization

The distribution, size and morphology of the as-prepared samples were characterized by scanning electron microscopy (SEM) (FEI SIRION 200). Transmission electron microscopy (TEM) and high-resolution TEM (HRTEM) measurements were conducted on a Philips-FEI Tecnai G2 F20 S-Twin microscope equipped with an energy dispersive X-ray (EDX) spectroscopy detector. The chemical compositions and structures of the as-

This journal is © The Royal Society of Chemistry 2015

J. Mater. Chem. A, 2015, **3**, 2762–2769 | **2763**

prepared samples were analysed by X-ray diffraction (XRD) (Bruker D8 Advance X-ray diffractometer, Cu-Kα radiation λ = 0.15406 nm) and X-ray photoelectron spectroscopy (XPS) (AXIS Ultra-DLD, Kratos Analytical, Manchester, UK, using mono-chromated Al Kα radiation). The exact Mo : Ti molar ratio (or weight percent, wt% of MoS_2 and TiO_2) in the nanocomposite was also measured by inductively coupled plasma optical emission spectroscopy (ICP-OES, Agilent 730). The $TiO_2@MoS_2$ nanocomposite sample was digested into the solution using a mixed acid method. Then the resulting solution was diluted appropriately and measured for the presence of Mo, S and Ti elements (molar ratio: Mo : S : Ti = 1.51 : 2.96 : 1) by ICP-OES.

Electrochemical measurements

The working electrodes were fabricated by coating a slurry containing 80 wt% of active materials ($TiO_2@MoS_2$ nano-composite, MoS_2 nanosheets, or TiO_2 nanowires), 10 wt% of acetylene black (Super-P), and 10 wt% of polyvinylidene fluoride (PVDF) dissolved in N-methyl-2-pyrrolidinone onto a copper foil and dried at 100 °C in vacuum for 12 h before pressing. Standard CR2032-type coin cells were assembled in an Ar-filled glovebox (KIYON, Korea) by using the as-prepared anode, Li metal foil (0.4 mm thick) as the counter electrode, and a separator (Solupor 7P03A). The electrolyte was 1 M $LiPF_6$ dissolved in a mixture of ethylene carbonate (EC) and dimethyl carbonate (DMC) (v/v = 1 : 1). The cells were aged for 12 h before the measurements. Galvanostatic discharge–charge (GDC) experiments were performed at different current densities in the voltage range of 0.01–3.00 V with a multichannel battery tester (Maccor, Inc, USA). Cyclic voltammetry (CV) measurements were conducted by using an electrochemical workstation (Solartron Potentiostat and Impedance Analyser, UK). Electrochemical impedance spectra (EIS) were recorded using the same electrochemical workstation by applying an AC voltage of 10 mV amplitude over the frequency range from 100 kHz to 100 mHz. Note that the specific capacity values were calculated on the basis of the total mass of the $TiO_2@MoS_2$ nanocomposite. The theoretical capacity of $TiO_2@MoS_2$ is calculated based on the ICP-OES result and a small amount of carbon is negligible. The battery GDC cycling and rate tests were performed with a mass loading of active electrode materials of 1.061 mg cm^{-2} and 1.085 mg cm^{-2}, respectively.

Results and discussion

The overall synthesis procedure of the $TiO_2@MoS_2$ nano-composite is illustrated in Fig. 1, which involves three steps. First, the TiO_2 nanowires were synthesized by the hydrothermal and ion exchange process followed by calcination in air. Then, the MoS_2 nanosheets grew on the surface of TiO_2 nanowires with the assistance of glucose through the hydrothermal reaction. Finally, the hydrothermal $TiO_2@MoS_2$ sample was treated at 800 °C under H_2/Ar gas to obtain the annealed $TiO_2@MoS_2$ nanocomposite.

The SEM image (Fig. S1a, ESI†) shows that the TiO_2-500 product is composed of elegant nanowires with lengths of
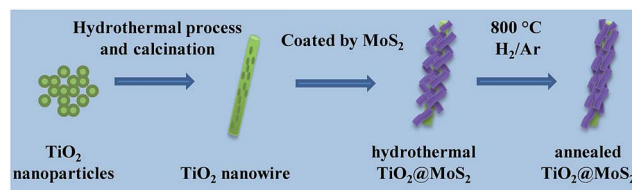

Fig. 1 Schematic illustration of the synthesis process of the $TiO_2@MoS_2$ nanocomposite.

several micrometers and diameters ranging from 50 to 200 nm. After undergoing a hydrothermal coating reaction, the surface of these nanowires becomes much rougher, indicating the successful growth of MoS_2 nanosheets onto TiO_2-500C nano-wires (Fig. 2a). The TEM image (Fig. 2b) shows that most MoS_2 nanosheets grow vertically on the 1D TiO_2 nanowires. After the thermal treatment at 800 °C, the $TiO_2@MoS_2$ nanocomposite
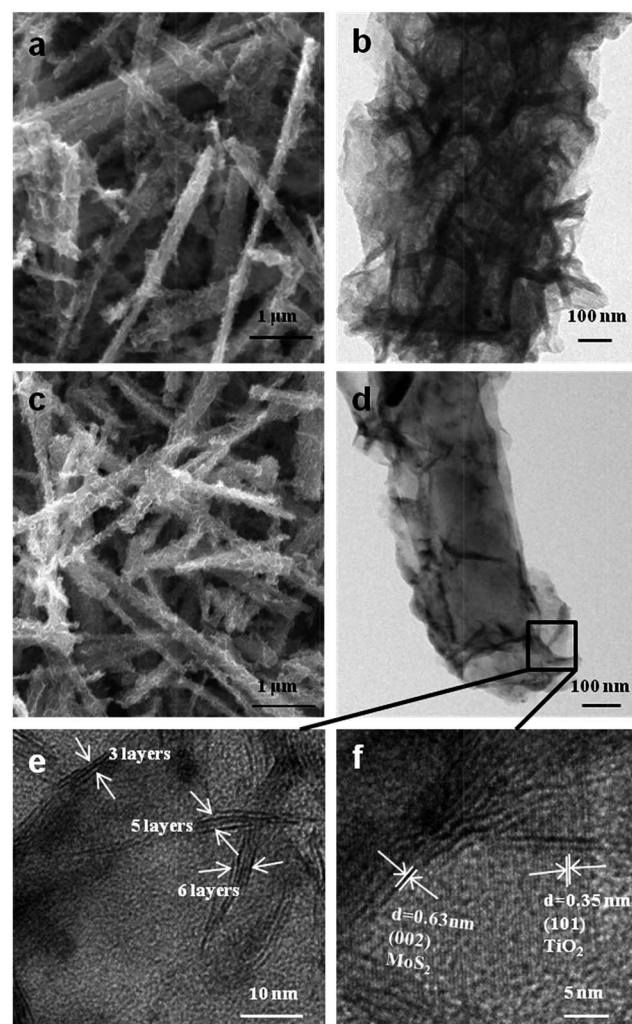

Fig. 2 SEM (a) and TEM (b) images of the hydrothermal $TiO_2@MoS_2$ nanocomposite; SEM (c) and TEM (d) images of the annealed $TiO_2@MoS_2$ nanocomposite; (e) and (f) HRTEM images of the annealed $TiO_2@MoS_2$ nanocomposite shown in the labelled area in 2d.

(Fig. 2c) still retains the 1D cable-sheath structure in which TiO_2 nanowires are uniformly covered by MoS_2 nanosheets. However, the core TiO_2 nanowires are more tightly wrapped by the annealed sheath-like MoS_2 nanosheets probably due to the shrinkage of the MoS_2 nanosheets caused by the high-temperature treatment (Fig. 2d).[19,36] Furthermore, the thin MoS_2 nanosheets on the TiO_2 nanowires backbone consist of few-layers (≤6 layers) (Fig. 2e) and the interlayer spacing of the MoS_2 nanosheets in the HRTEM image (Fig. 2f) is approximately 0.63 nm corresponding to the (002) plane of the hexagonal 2H-MoS_2 (JCPDS Card no. 37-1492). The lattice fringe of 0.35 nm is consistent with the (101) plane of anatase TiO_2 (JCPDS Card no. 21-1272). For the pure MoS_2 sample, MoS_2 nanosheets aggregate to form MoS_2 nanoparticles (Fig. S1b, ESI†). In contrast to the bare MoS_2 agglomerated particles, sheath-like MoS_2 nanosheets in the TiO_2@MoS_2 nanocomposite are unfolded and thus expose more surface active sites, which can promote a rapid charge-transfer reaction and facilitate Li^+ migration for the LIBs.

The structures and chemical compositions of the samples were examined by X-ray diffraction (XRD) (Fig. 3) and energy dispersive X-ray spectroscopy (EDX) (Fig. S2, ESI†). The XRD pattern of TiO_2-500C indicates that they are a mixture of TiO_2 (B) (JCPDS Card no. 74-1940) and anatase phase (JCPDS Card no. 21-1272). After the hydrothermal coating reaction, the diffraction peaks of MoS_2 appear and the intensities of TiO_2 peaks decrease, indicating successful coating of the MoS_2 sheath in the TiO_2@MoS_2 nanocomposite. After annealing, mixed phase TiO_2 nanowires are completely converted to the anatase phase, and most of the diffraction peaks become intense and sharpen, due to the crystallization of the nanocomposite at 800 °C. Note that the nanocomposite samples do not exhibit a (002) diffraction peak of MoS_2 that is typically observed at 14.5° in the bulk analogue. This suggests that the

MoS_2 nanosheets in the nanocomposites only contain few layers (≤6 layers), which are too thin to be detected by XRD.[13,38] This is in good agreement with the TEM observation. The EDX spectrum of many TiO_2@MoS_2 nanowires (Fig. S2, ESI†) further confirms the presence of TiO_2 and MoS_2 in the hierarchical nanocomposite and the Mo : Ti molar ratio is about 1.48 : 1. This is consistent with the ICP-OES result of the Mo : Ti molar ratio of 1.51 : 1 (i.e. 75 wt% of MoS_2 and 25 wt% of TiO_2 in the nanocomposite).

X-ray photoelectron spectroscopy (XPS) was employed to further investigate the chemical states of elements on the surface of hydrothermal and annealed TiO_2@MoS_2 nanocomposites. The full XPS survey shows that Mo, S, Ti and O elements coexist in the as-prepared TiO_2@MoS_2 nanocomposites (Fig. S3a, ESI†), and the XPS peak for extra C 1s is ascribed to carbon components within the nanocomposite. The XPS peaks for Ti 2p are relatively weak (Fig. S3b, ESI†), indicating the uniformly thick coverage of the MoS_2 sheath. For bare TiO_2 nanowires, the C 1s peak arises primarily from inevitable carbon contamination. By comparison, the intensity of the C 1s peak for either the hydrothermal or annealed TiO_2@MoS_2 nanocomposite is significantly increased, indicating that carbon is doped in the nanocomposites. The carbon component in the hydrothermal nanocomposite is likely to come from residual glucose hydrocarbon groups. After annealing, the C 1s peak slightly shifts to the lower binding energy position due to the formation of C–C during carbonization of the carbon component in the nanocomposite at 800 °C.[39] The carbon component would enhance the electrical conductivity (Fig. S5, ESI†) and rate capability (Fig. S4, ESI†) of the nanocomposites, which is in agreement with the observation in the reported silicon nanowires coated with the carbon-doped TiO_2 shell.[40] The high-resolution XPS spectra (Fig. 4a and b) show that the binding energies of Mo $3d_{5/2}$, Mo $3d_{3/2}$, S $2p_{3/2}$ and S $2p_{1/2}$ peaks in the annealed TiO_2@MoS_2 nanocomposite are located at 229.5, 232.7, 162.4 and 163.5 eV respectively, which is consistent with those of reported MoS_2.[19,36] In the case of the hydrothermal TiO_2@MoS_2 hybrid nanostructure, these peaks are broadened, and shift towards the lower binding energy by ca. 0.7 eV (228.8, 232, 161.7, and 162.8 eV respectively). The broadened peaks indicate that a variety of molybdenum oxides and sulphides exist in the hydrothermal product in addition to MoS_2. These are usually observed in MoS_2–graphene composites and bulk MoS_2.[25] The shift of these peaks can be attributed
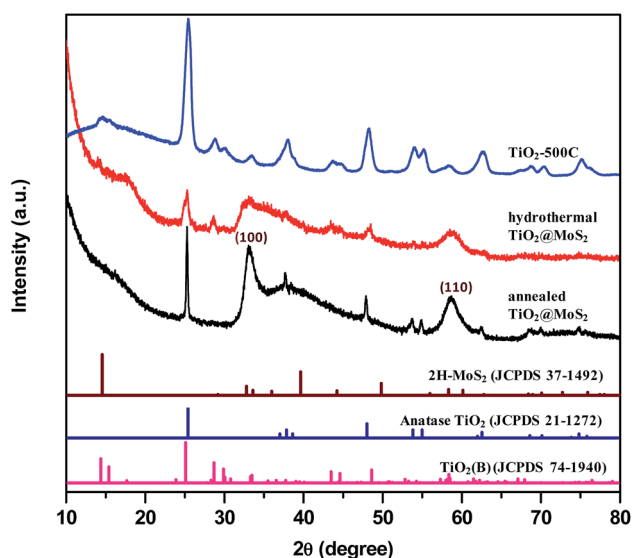

Fig. 3 XRD patterns of TiO_2-500C, the hydrothermal TiO_2@MoS_2 nanocomposite and the annealed TiO_2@MoS_2 nanocomposite as well as the standard JCPDS cards of TiO_2 and MoS_2.
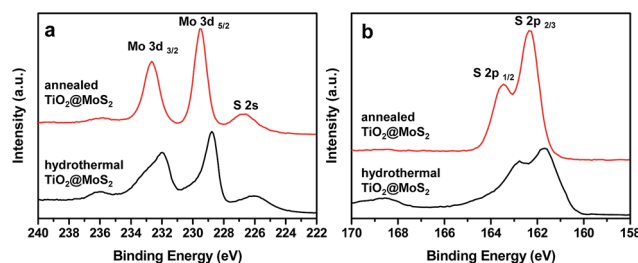

Fig. 4 XPS spectra of hydrothermal and annealed TiO_2@MoS_2 nanocomposites; (a) Mo 3d and S 2s peaks and (b) S 2p peaks.

to the heterostructure effect between the MoS_2 nanosheets and the TiO_2 backbone.[37,38] Thus, for $TiO_2@MoS_2$ nanocomposites, the annealing process under H_2/Ar gas could improve the purity of MoS_2 and reduce the interference of other materials.

We investigated the effect of glucose and surface roughness on the morphology of hybrid nanostructures. The TEM image of TiO_2-500C displays their porosity, indicating that TiO_2-500C possesses a naturally rough surface (Fig. 5a). To study the role of glucose, a controlled sample was synthesized by employing TiO_2-500C without the addition of glucose. Fig. 5b illustrates that few MoS_2 nanosheets are coated onto the surface of TiO_2-500C. Most of the micro-sized MoS_2 sheets aggregate into thick flakes. As shown in Fig. 5c, the surface of TiO_2-800C is much smoother than that of TiO_2-500C, possibly because of the re-crystallization during the high-temperature treatment. When such TiO_2-800C was used as the backbone, even with the assistance of glucose, few MoS_2 nanosheets grew on the surface of TiO_2 nanowires (Fig. 5d). Excess small MoS_2 nanosheet units tend to aggregate into discrete microspheres. Based on these results, it is clear that both glucose and roughness of the TiO_2 backbone are crucial for the formation of the uniform $TiO_2@MoS_2$ nanocomposite. The rough surface of TiO_2 nanowires can provide more accessible active sites for the nucleation and growth of MoS_2 nanosheets, while glucose is able to suppress the growth and stack of layered MoS_2 with large size, mediate the formation of uniform MoS_2 nanosheets with smaller size and thickness and act as a binder to promote the MoS_2 nanosheets to grow on the surface of TiO_2 nanowires with uniform coverage along the longitudinal direction.[18,36,38]
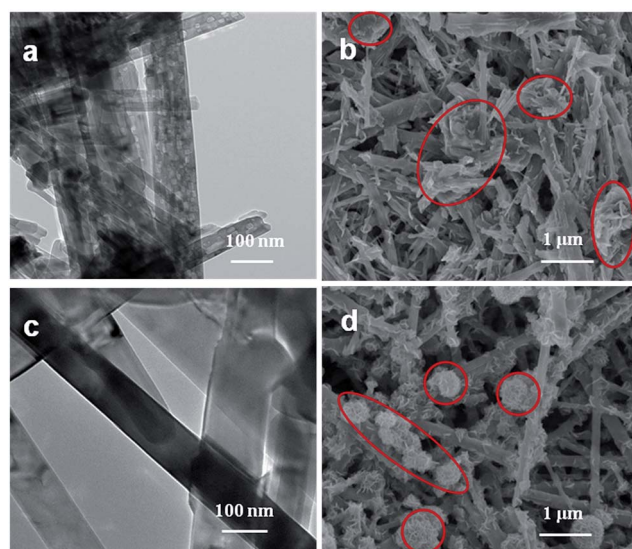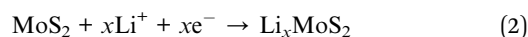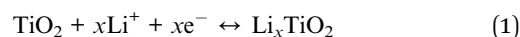
Application as a Li-ion battery anode

The annealed $TiO_2@MoS_2$ nanocomposite was then assembled into Li half-cells to investigate the electrochemical performance. Fig. 6a shows the cyclic voltammetry curves (CVs) of the annealed $TiO_2@MoS_2$ nanocomposite, which were collected at a slow scan rate of 0.05 mV s^{-1} in a potential window of 0.01–3.0 V vs. Li$^+$/Li. In the first cathodic process (discharge process), three reduction peaks appear at approximately 1.72 V, 1.1 V and 0.6 V. The weak cathodic peak at 1.72 V is due to the lithiation of TiO_2 nanowires (Reaction 1).[34] The cathodic peak at 1.1 V is attributed to the Li intercalation into the layered MoS_2, resulting in the phase transformation from 2H-MoS_2 to 1T Li$_x$MoS$_2$ (Reaction 2).[14,24] The cathodic peak at 0.6 V can be assigned to further decomposition of Li$_x$MoS$_2$ into Li$_2$S and Mo (Reaction 3).[14,23] The electrochemical reactions of the $TiO_2@MoS_2$ nanocomposite in the first discharge process occur as follows:[14,30]

$$TiO_2 + xLi^+ + xe^- \leftrightarrow Li_xTiO_2 \tag{1}$$

$$MoS_2 + xLi^+ + xe^- \rightarrow Li_xMoS_2 \tag{2}$$

$$Li_xMoS_2 + (4-x)Li^+ + (4-x)e^- \rightarrow Mo + 2Li_2S \tag{3}$$

In the first charge process, three anodic peaks appear at ~1.75 V, ~2.07 V and ~2.3 V, respectively. The small anodic peak at 1.75 V is likely due to the delithiation of residual Li$_x$MoS$_2$ that has not been converted to Mo and Li$_2$S. The two peaks at ~2.07 V and ~2.3 V are assigned to two reversible conversion reactions of Li$_x$TiO$_2$ to TiO$_2$ and Li$_2$S to S$_8$, respectively.

Fig. 5 (a) TEM image of rough TiO_2-500C nanowires, (b) SEM image of the TiO_2–MoS_2 composite by using rough TiO_2-500C without the addition of glucose, (c) TEM image of smooth TiO_2-800C nanowires and (d) SEM image of the TiO_2–MoS_2 composite by using smooth TiO_2-800C with the addition of glucose. For clarity, the MoS_2 agglomerates are marked in (b) and (d).
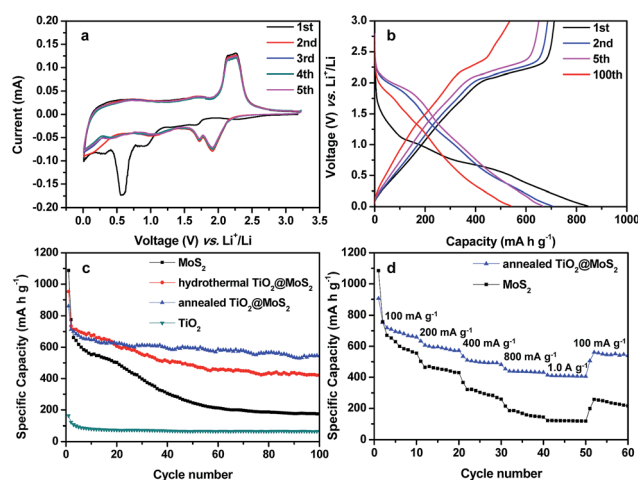

Fig. 6 (a) Representative CV curves for the 1st, 2nd, 3rd, 4th and 5th cycle of the annealed $TiO_2@MoS_2$ nanocomposite at a scan rate of 0.05 mV s^{-1}, (b) galvanostatic charge–discharge voltage profiles of the annealed $TiO_2@MoS_2$ nanocomposite at a current density of 100 mA g^{-1}, (c) comparative cycling performance of bare MoS_2 nanosheets, bare TiO_2 nanowires, the hydrothermal $TiO_2@MoS_2$ nanocomposite and the annealed $TiO_2@MoS_2$ nanocomposite at a current density of 100 mA g^{-1}, and (d) rate performance of the annealed $TiO_2@MoS_2$ nanocomposite and pure MoS_2 nanoparticles at different current densities.

2766 | J. Mater. Chem. A, 2015, **3**, 2762–2769

This journal is © The Royal Society of Chemistry 2015

Differently, in subsequent cycles, a new cathodic peak at approximately 1.9 V is apparently observed while the peaks at 1.1 and 0.6 V as previously discussed are diminished. The dominant cathodic peak forming at ~1.9 V is well known in lithium–sulfur battery systems and is attributed to the formation of Li_2S.[41,42]

In order to further investigate the lithium ion storage performance of the electrodes, the discharge–charge measurements were carried out at a current density of 100 mA g^{-1} for 100 cycles. For comparison, the hydrothermal $TiO_2@MoS_2$ nanocomposite, bare TiO_2 nanowires and MoS_2 particles were also tested. Fig. 6b presents the galvanostatic discharge–charge (GDC) voltage profiles of the annealed $TiO_2@MoS_2$ nanocomposite at 100 mA g^{-1}. Upon initial discharge, the small sloped profile at >1.5 V corresponds to the lithiation of TiO_2 (Reaction 1), and two apparent voltage plateaus at 1.0 and 0.6 V are attributed to the phase transformation from 2H-MoS_2 to 1T Li_xMoS_2 (Reaction 2) and further conversion into Mo and Li_2S (Reaction 3), respectively. These GDC results are well consistent with the CV results. The subsequent GDC cycles demonstrate slow sloped profiles, with plateaus at around 2.0 V and 2.3 V upon discharge and charge, primarily corresponding to the reversible electrochemical processes of Li_2S. The initial discharge and charge specific capacities are 862 and 724 mA h g^{-1}, respectively, leading to a relatively high Coulombic efficiency (CE) of 84%, which is higher than those of MoS_2–carbon nanofiber, MoS_2–carbon nanotube and MoS_2–graphene composites.[18–24] Comparatively, the initial CEs of bare MoS_2 nanosheets, bare TiO_2 nanowires and hydrothermal $TiO_2@MoS_2$ nanocomposite are merely 76.7%, 76.8% and 80.1%, respectively, which demonstrates the favourable synergistic effect of the annealed $TiO_2@MoS_2$ nanocomposite (Fig. S4, ESI†). As the initial irreversible capacity loss is largely due to the formation of SEI, the improvement of CE for the hydrothermal or annealed $TiO_2@MoS_2$ nanocomposite over that of either single component is primarily attributed to the MoS_2 sheath that wraps the core TiO_2 nanowire. In addition, the MoS_2 sheath is able to wrap the core TiO_2 nanowire more tightly in the annealed $TiO_2@MoS_2$ nanocomposite compared to the hydrothermal counterpart (Fig. 2), hereby resulting in a higher CE. Therefore, these results demonstrate that such a unique hybrid nanostructure could effectively inhibit the side reactions by decreasing the detrimental contact with the electrolyte, highlighting the synergistic effect of the nanocomposite. The CE of the annealed $TiO_2@MoS_2$ nanocomposite quickly stabilizes at approximately 98% from the second cycle (Fig. S4a, ESI†).

The $TiO_2@MoS_2$ nanocomposite also exhibits enhanced cycling stability and rate performance. Fig. S4† displays the cycling and rate performances of the annealed $TiO_2@MoS_2$ nanocomposite, hydrothermal $TiO_2@MoS_2$ nanocomposite, bare MoS_2 nanosheets and TiO_2 nanowires. They are compared more clearly in Fig. 6c and d. The specific capacity of the bare TiO_2 nanowires decreases quickly from 164 mA h g^{-1} to 66 mA h g^{-1} at 100 mA g^{-1} after 50 cycles. Similarly, the capacity of bare MoS_2 dramatically fades from 1088 mA h g^{-1} to 175 mA h g^{-1} at 100 mA g^{-1} after 100 cycles. Apparently, both of them suffer from severe capacity degradation upon charge–discharge

cycling. On one hand, a large volume change normally occurs in MoS_2 based materials (~103%) during lithium ion insertion and extraction.[14] On the other hand, the TiO_2 nanowires or MoS_2 nanoparticles tend to aggregate and pulverize, which will cause electrical disconnection from current collectors. In contrast, both hydrothermal and annealed $TiO_2@MoS_2$ nanocomposites show significantly enhanced cycling stability. Especially, the annealed $TiO_2@MoS_2$ nanocomposite shows higher cycling stability than the hydrothermal $TiO_2@MoS_2$ counterpart, possibly due to its stronger affinity between the MoS_2 sheath and the TiO_2 nanowire core (Fig. 6c). The annealed $TiO_2@MoS_2$ electrodes still can retain a capacity of 544 mA h g^{-1} after 100 cycles, which equals 93% of the theoretical capacity of the $TiO_2@MoS_2$ nanocomposite according to the calculation as follows:[33,36]

$$C_{TiO_2@MoS_2} = C_{MoS_2} \times wt\%_{MoS_2} + C_{TiO_2} \times wt\%_{TiO_2} = 670 \times 0.75 + 335 \times 0.25 = 586 \text{ mA h } g^{-1}$$

Note that the theoretical capacity of MoS_2 was reported to be 670 mA h g^{-1}, which was calculated on the basis of the balanced reaction of $MoS_2 + 4Li \leftrightarrow Mo + 2Li_2S$, as per the conversion reaction.[13] Herein, this value was also used in the above equation. However, the observed capacities of MoS_2 were found to be higher than 670 mA h g^{-1} in the literature.[13,36] In this study, the reversible capacity of the $TiO_2@MoS_2$ nanocomposite is also higher than the calculated theoretical capacity of 586 mA h g^{-1}, which is probably caused by the different electrochemical lithium ion storage mechanisms of the MoS_2 nanosheets from the conversion reaction. As shown in the CV curves (Fig. 6a), the conversion reaction occurred in the first cycle. After that, the dominant reversible electrochemical reaction occurred between sulfur and Li, the same as the Li–S batteries, which contributes to higher reversible capacities of the $TiO_2@MoS_2$ nanocomposite in the subsequent cycles than the theoretical capacity based on the conversion reaction.

The synergistic effect between the TiO_2 nanowires and MoS_2 nanosheets is confirmed, since the composite capacities significantly exceed those of either individual component. Furthermore, the annealed $TiO_2@MoS_2$ nanocomposite anode shows improved rate capability (Fig. 6d and S4†). Even at 1000 mA g^{-1}, it still delivers a high specific capacity of 414 mA h g^{-1}, while the bare MoS_2 and TiO_2 can only deliver the capacity of 120 mA h g^{-1} and 23 mA h g^{-1}, respectively, at the same current density. When the current density is back to 100 mA g^{-1}, the capacity of the annealed $TiO_2@MoS_2$ nanocomposite returns to 563 mA h g^{-1}, indicating the good capacity recovery.

In order to understand the superior electrochemical performance of the $TiO_2@MoS_2$ nanocomposite, EIS (Fig. S5, ESI†) measurements were carried out for the annealed $TiO_2@MoS_2$ nanocomposite, bare TiO_2 nanowires and MoS_2 nanosheets before battery cycling tests and after 100 cycles. A whole Nyquist plot is composed of one semicircle whose diameter represents the charge transfer resistance at the high frequency zone, followed by a slope line at the low frequency region. Compared to bare TiO_2 and MoS_2, the $TiO_2@MoS_2$ nanocomposite shows a

smaller semicircle diameter before and after cycling, indicating that TiO$_2$@MoS$_2$ has lower charge transfer resistance. Thus, the TiO$_2$@MoS$_2$ nanocomposite demonstrates enhanced kinetic performance, cycling stability and improved conductivity and Coulombic efficiency, highlighting the synergistic effect (Fig. S5, ESI†).[40,43]

The structure and morphology of TiO$_2$@MoS$_2$ were further characterized to confirm the backbone robustness by SEM after 100 cycles (Fig. S6, ESI†). The TiO$_2$@MoS$_2$ nanocomposite still retained its original 1D hierarchical nanostructure, demonstrating that the robust TiO$_2$ backbone structure can withstand the stress of volume changes and prevent pulverization during the discharge–charge cycles.

The synergistic effect and the structural advantages of the TiO$_2$@MoS$_2$ nanocomposite contribute to the excellent cycling stability and remarkable rate capability. First, the carbon-doped TiO$_2$ nanowire core enables fast electronic transportation to the ultrathin MoS$_2$ and the MoS$_2$ sheath offers efficient Li$^+$ supply for the TiO$_2$ nanowire core, facilitating Li storage kinetics and collaborative stability. Second, the interconnected robust one-dimensional structure of the carbon-doped TiO$_2$ nanowire backbone could effectively accommodate the strain of the volume change of MoS$_2$ and maintain the hierarchically conductive network, which brings about excellent cycling stability even at high rates. Third, the affinity between MoS$_2$ nanosheets and TiO$_2$ nanowires restrains the aggregation and pulverization of MoS$_2$ upon lithiation/delithiation. Last, ultra-thin MoS$_2$ nanosheets provide high electrode/electrolyte interfacial contact areas and shorten the Li$^+$ diffusion paths for rapid charge transfer. Thus, the composite structure is able to form a stable SEI quickly and prevents the electrolyte from further decomposition, leading to rapid stabilization of CE at around 99%. The few-layered and crystalline MoS$_2$ sheath contributes the most to the high capacity of the nanocomposite for lithium ion storage through the two-step reaction (Reaction 2 & 3). Therefore, it is the synergism of the TiO$_2$ backbone and MoS$_2$ sheath components that leads to a superior anode composite material for high-capacity, fast and stable LIBs. This strategy will also be applied to other core-sheath composite nanostructures for promising Na/Mg ion batteries, by rational design of the components of the core (*e.g.* carbon nanofibers, Li$_4$Ti$_5$O$_{12}$, *etc.*) and sheath (*e.g.* WS$_2$, WSe$_2$, *etc.*).

Conclusions

In summary, a hierarchical nanocomposite of 1D robust TiO$_2$ nanowires coated with molybdenum disulfide nanosheets (TiO$_2$@MoS$_2$) has been successfully developed by a simple and cost-effective glucose-assisted hydrothermal method. The robust TiO$_2$ nanowires act as the effective backbone for the nucleation and growth of ultrathin MoS$_2$ nanosheets (≤ 6 layers). Both the glucose and roughness of the TiO$_2$ backbone play critical roles in the uniform coating of MoS$_2$ nanosheets onto the TiO$_2$ nanowires. As the anode materials for LIBs, the cooperation of the two active components in the TiO$_2$@MoS$_2$ nanocomposite generates a favourable synergistic effect on the electrochemical lithium storage. The robust carbon-doped TiO$_2$ nanowire backbone offers an efficient pathway for electron and lithium ion transport, and effectively accommodates the volume changes, while ultrathin MoS$_2$ nanosheets provide high electrode/electrolyte interfacial contact areas, shorten the diffusion length, promote lithiation/delithiation kinetics and contribute to the high specific capacities. The synergistic effect leads to enhanced specific capacity, improved cycling stability and superior rate capability of the nanocomposite. The TiO$_2$@MoS$_2$ nanocomposite exhibits a high initial discharge capacity of 862 mA h g^{-1} with a high initial Coulombic efficiency of 84% at 100 mA g^{-1}. The discharge capacity still remains at 544 mA h g^{-1} with the Coulombic efficiency of over 99% after 100 cycles. The TiO$_2$@MoS$_2$ nanocomposite also displays an excellent rate performance (414 mA h g^{-1} at 1000 mA g^{-1}), making it a promising anode material for high performance LIBs. Moreover, this work provides insight into the synergistic effect in nanocomposite electrodes and opens up an avenue for the rational design of other anode composite materials in high performance LIBs.

Acknowledgements

References

1 N.-S. Choi, Z. Chen, S. A. Freunberger, X. Ji, Y.-K. Sun, K. Amine, G. Yushin, L. F. Nazar, J. Cho and P. G. Bruce, *Angew. Chem., Int. Ed.*, 2012, **51**, 9994.

2 M. Armand and J. M. Tarascon, *Nature*, 2008, **451**, 652.

3 B. Dunn, H. Kamath and J.-M. Tarascon, *Science*, 2011, **334**, 928.

4 J. B. Goodenough and K.-S. Park, *J. Am. Chem. Soc.*, 2013, **135**, 1167.

5 W. Li, Y.-X. Yin, S. Xin, W.-G. Song and Y.-G. Guo, *Energy Environ. Sci.*, 2012, **5**, 8007.

6 L.-S. Zhang, L.-Y. Jiang, C.-Q. Chen, W. Li, W.-G. Song and Y.-G. Guo, *Chem. Mater.*, 2009, **22**, 414.

7 M. V. Reddy, G. V. Subba Rao and B. V. R. Chowdari, *Chem. Rev.*, 2013, **113**, 5364.

8 C. Liu, F. Li, L.-P. Ma and H.-M. Cheng, *Adv. Mater.*, 2010, **22**, E28.

9 W. Li, C.-Y. Cao, C.-Q. Chen, Y. Zhao, W.-G. Song and L. Jiang, *Chem. Commun.*, 2011, **47**, 3619.

10 S. Xin, Y.-G. Guo and L.-J. Wan, *Acc. Chem. Res.*, 2012, **45**, 1759.

2768 | *J. Mater. Chem. A*, 2015, **3**, 2762–2769

This journal is © The Royal Society of Chemistry 2015

11 H. Liu, D. Su, G. Wang and S. Z. Qiao, *J. Mater. Chem.*, 2012, **22**, 17437.

12 C. Xu, Y. Zeng, X. Rui, N. Xiao, J. Zhu, W. Zhang, J. Chen, W. Liu, H. Tan, H. H. Hng and Q. Yan, *ACS Nano*, 2012, **6**, 4713.

13 H. Hwang, H. Kim and J. Cho, *Nano Lett.*, 2011, **11**, 4826.

14 T. Stephenson, Z. Li, B. Olsen and D. Mitlin, *Energy Environ. Sci.*, 2014, **7**, 209.

15 C. Feng, J. Ma, H. Li, R. Zeng, Z. Guo and H. Liu, *Mater. Res. Bull.*, 2009, **44**, 1811.

16 R. Dominko, D. Arčon, A. Mrzel, A. Zorko, P. Cevc, P. Venturini, M. Gaberscek, M. Remskar and D. Mihailovic, *Adv. Mater.*, 2002, **14**, 1531.

17 H. Li, W. Li, L. Ma, W. Chen and J. Wang, *J. Alloys Compd.*, 2009, **471**, 442.

18 S. Ding, J. S. Chen and X. W. Lou, *Chem.–Eur. J.*, 2011, **17**, 13142.

19 Y. Shi, Y. Wang, J. I. Wong, A. Y. S. Tan, C.-L. Hsu, L.-J. Li, Y.-C. Lu and H. Y. Yang, *Sci. Rep.*, 2013, **3**, 1.

20 F. Zhou, S. Xin, H.-W. Liang, L.-T. Song and S.-H. Yu, *Angew. Chem., Int. Ed.*, 2014, **53**, 11552.

21 C. Zhu, X. Mu, P. A. van Aken, Y. Yu and J. Maier, *Angew. Chem., Int. Ed.*, 2014, **53**, 2152.

22 X. Xu, Z. Fan, X. Yu, S. Ding, D. Yu and X. W. Lou, *Adv. Energy Mater.*, 2014, DOI: 10.1002/aenm.201400902.

23 X. Zhou, L.-J. Wan and Y.-G. Guo, *Chem. Commun.*, 2013, **49**, 1838.

24 K. Chang and W. Chen, *ACS Nano*, 2011, **5**, 4720.

25 Y. Gong, S. Yang, Z. Liu, L. Ma, R. Vajtai and P. M. Ajayan, *Adv. Mater.*, 2013, **25**, 3979.

26 L. Yang, S. Wang, J. Mao, J. Deng, Q. Gao, Y. Tang and O. G. Schmidt, *Adv. Mater.*, 2013, **25**, 1180.

27 M. Wagemaker, G. J. Kearley, A. A. van Well, H. Mutka and F. M. Mulder, *J. Am. Chem. Soc.*, 2002, **125**, 840.

28 J. S. Chen, Y. L. Tan, C. M. Li, Y. L. Cheah, D. Luan, S. Madhavi, F. Y. C. Boey, L. A. Archer and X. W. Lou, *J. Am. Chem. Soc.*, 2010, **132**, 6124.

29 D. Deng, M. G. Kim, J. Y. Lee and J. Cho, *Energy Environ. Sci.*, 2009, **2**, 818.

30 Y. Ren, Z. Liu, F. Pourpoint, A. R. Armstrong, C. P. Grey and P. G. Bruce, *Angew. Chem., Int. Ed.*, 2012, **124**, 2206.

31 F.-F. Cao, Y.-G. Guo, S.-F. Zheng, X.-L. Wu, L.-Y. Jiang, R.-R. Bi, L.-J. Wan and J. Maier, *Chem. Mater.*, 2010, **22**, 1908.

32 J.-H. Jeun, K.-Y. Park, D.-H. Kim, W.-S. Kim, H.-C. Kim, B.-S. Lee, H. Kim, W.-R. Yu, K. Kang and S.-H. Hong, *Nanoscale*, 2013, **5**, 8480.

33 J. Luo, X. Xia, Y. Luo, C. Guan, J. Liu, X. Qi, C. F. Ng, T. Yu, H. Zhang and H. J. Fan, *Adv. Energy Mater.*, 2013, **3**, 737.

34 X. Zhang, H. Chen, Y. Xie and J. Guo, *J. Mater. Chem. A*, 2014, **2**, 3912.

35 Y. Luo, J. Luo, W. Zhou, X. Qi, H. Zhang, D. Y. W. Yu, C. M. Li, H. J. Fan and T. Yu, *J. Mater. Chem. A*, 2013, **1**, 273.

36 X. Xu, Z. Fan, S. Ding, D. Yu and Y. Du, *Nanoscale*, 2014, **6**, 5245.

37 M. Mao, L. Mei, D. Guo, L. Wu, D. Zhang, Q. Li and T. Wang, *Nanoscale*, 2014, **6**, 12350.

38 W. Zhou, Z. Yin, Y. Du, X. Huang, Z. Zeng, Z. Fan, H. Liu, J. Wang and H. Zhang, *Small*, 2013, **9**, 140.

39 W. Li, L.-S. Zhang, Q. Wang, Y. Yu, Z. Chen, C.-Y. Cao and W.-G. Song, *J. Mater. Chem.*, 2012, **22**, 15342.

40 E. Memarzadeh Lotfabad, P. Kalisvaart, K. Cui, A. Kohandehghan, M. Kupsta, B. Olsen and D. Mitlin, *Phys. Chem. Chem. Phys.*, 2013, **15**, 13646.

41 X. Ji, K. T. Lee and L. F. Nazar, *Nat. Mater.*, 2009, **8**, 500.

42 Y.-X. Wang, L. Huang, L.-C. Sun, S.-Y. Xie, G.-L. Xu, S.-R. Chen, Y.-F. Xu, J.-T. Li, S.-L. Chou, S.-X. Dou and S.-G. Sun, *J. Mater. Chem.*, 2012, **22**, 4744.

43 E. L. Memarzadeh, W. P. Kalisvaart, A. Kohandehghan, B. Zahiri, C. M. B. Holt and D. Mitlin, *J. Mater. Chem.*, 2012, **22**, 6655.

This journal is © The Royal Society of Chemistry 2015

J. Mater. Chem. A, 2015, **3**, 2762–2769 | **2769**